

This figure "f1.jpg" is available in "jpg" format from:

<http://arxiv.org/ps/astro-ph/9703092v1>

This figure "f2.jpg" is available in "jpg" format from:

<http://arxiv.org/ps/astro-ph/9703092v1>

This figure "f3.jpg" is available in "jpg" format from:

<http://arxiv.org/ps/astro-ph/9703092v1>

This figure "f4.jpg" is available in "jpg" format from:

<http://arxiv.org/ps/astro-ph/9703092v1>

This figure "f5a.jpg" is available in "jpg" format from:

<http://arxiv.org/ps/astro-ph/9703092v1>

This figure "f5b.jpg" is available in "jpg" format from:

<http://arxiv.org/ps/astro-ph/9703092v1>

This figure "f5c.jpg" is available in "jpg" format from:

<http://arxiv.org/ps/astro-ph/9703092v1>

This figure "f6a.jpg" is available in "jpg" format from:

<http://arxiv.org/ps/astro-ph/9703092v1>

This figure "f6b.jpg" is available in "jpg" format from:

<http://arxiv.org/ps/astro-ph/9703092v1>

This figure "f6c.jpg" is available in "jpg" format from:

<http://arxiv.org/ps/astro-ph/9703092v1>

This figure "f7a.jpg" is available in "jpg" format from:

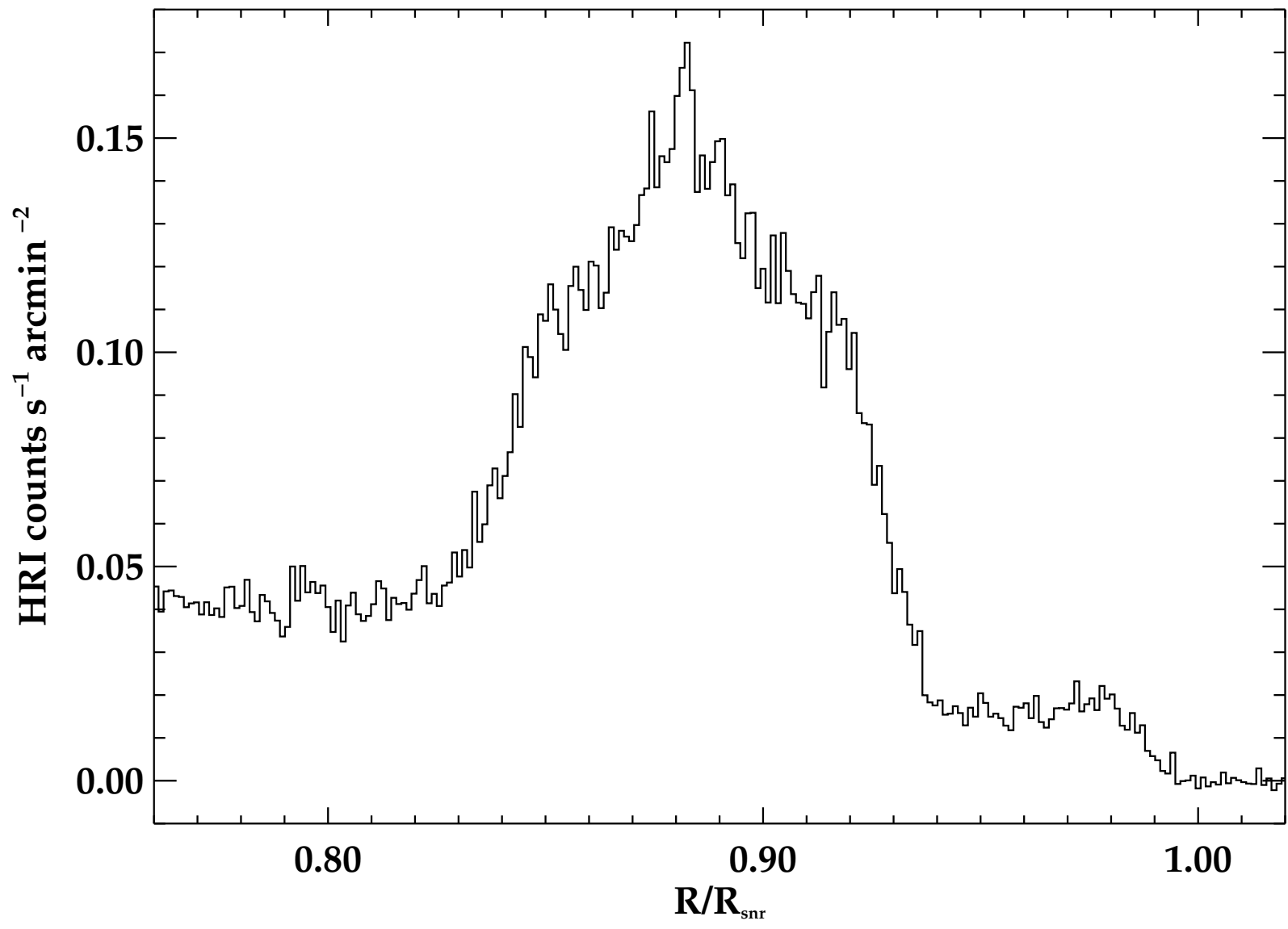
<http://arxiv.org/ps/astro-ph/9703092v1>

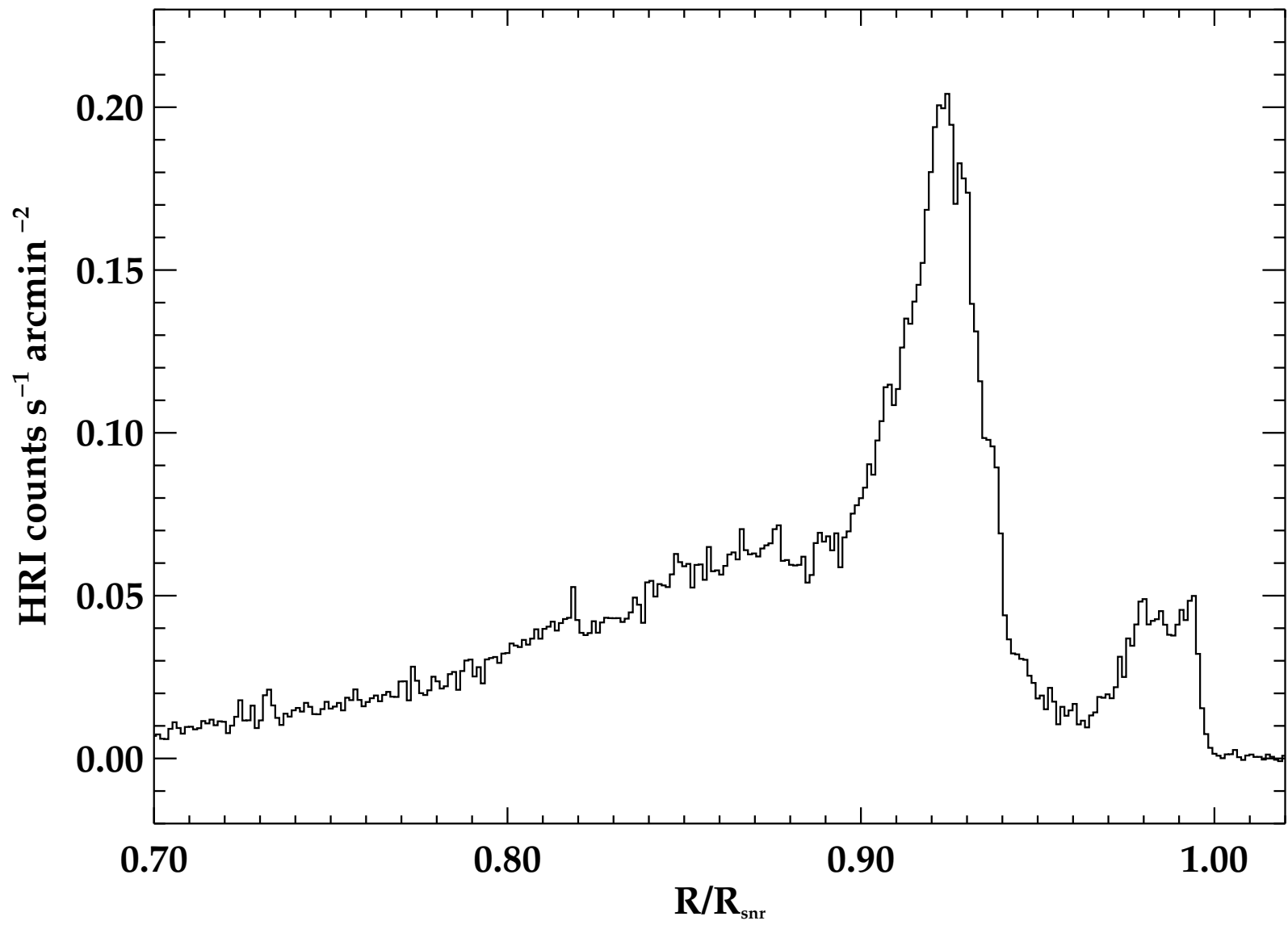
This figure "f7b.jpg" is available in "jpg" format from:

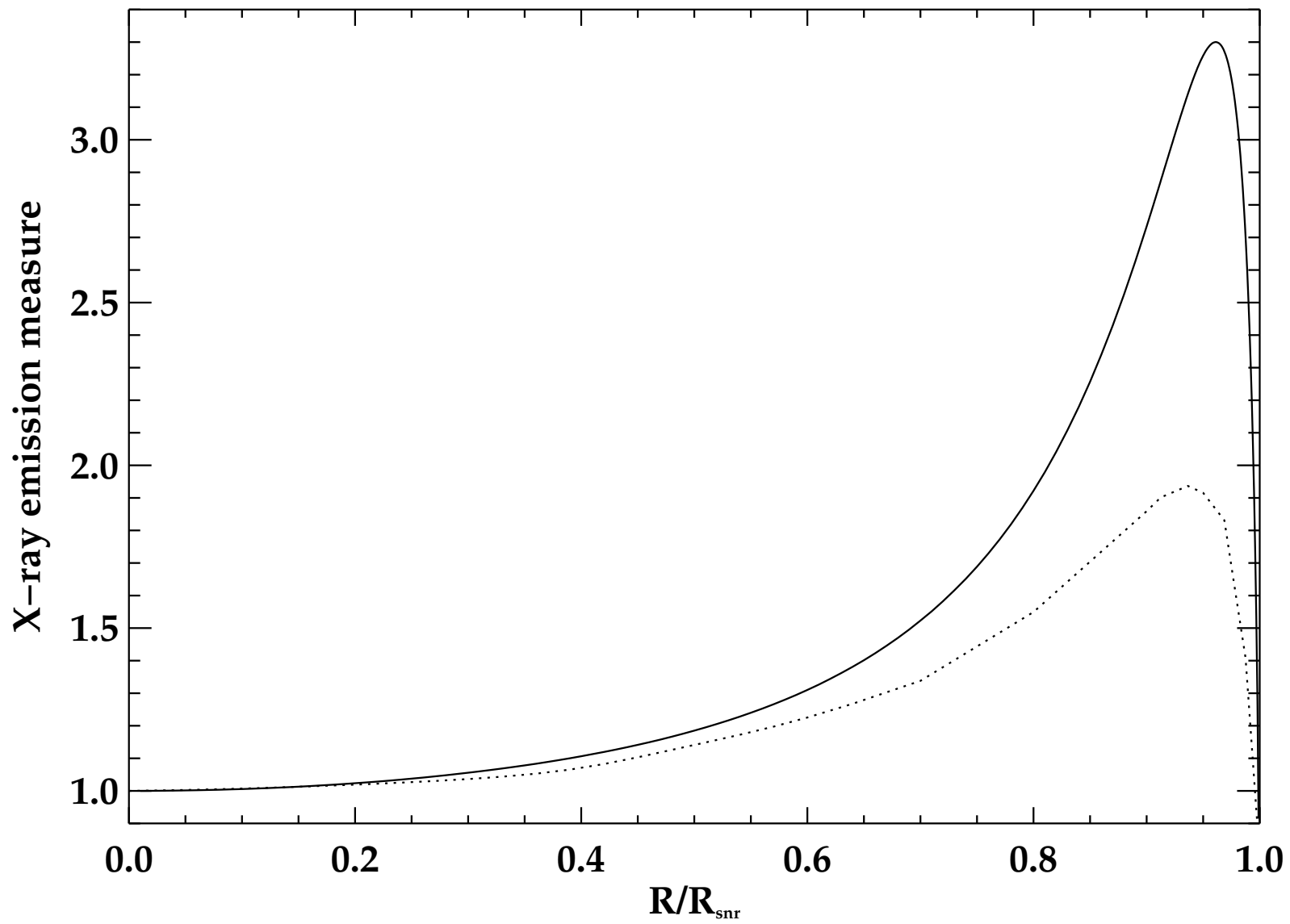
<http://arxiv.org/ps/astro-ph/9703092v1>

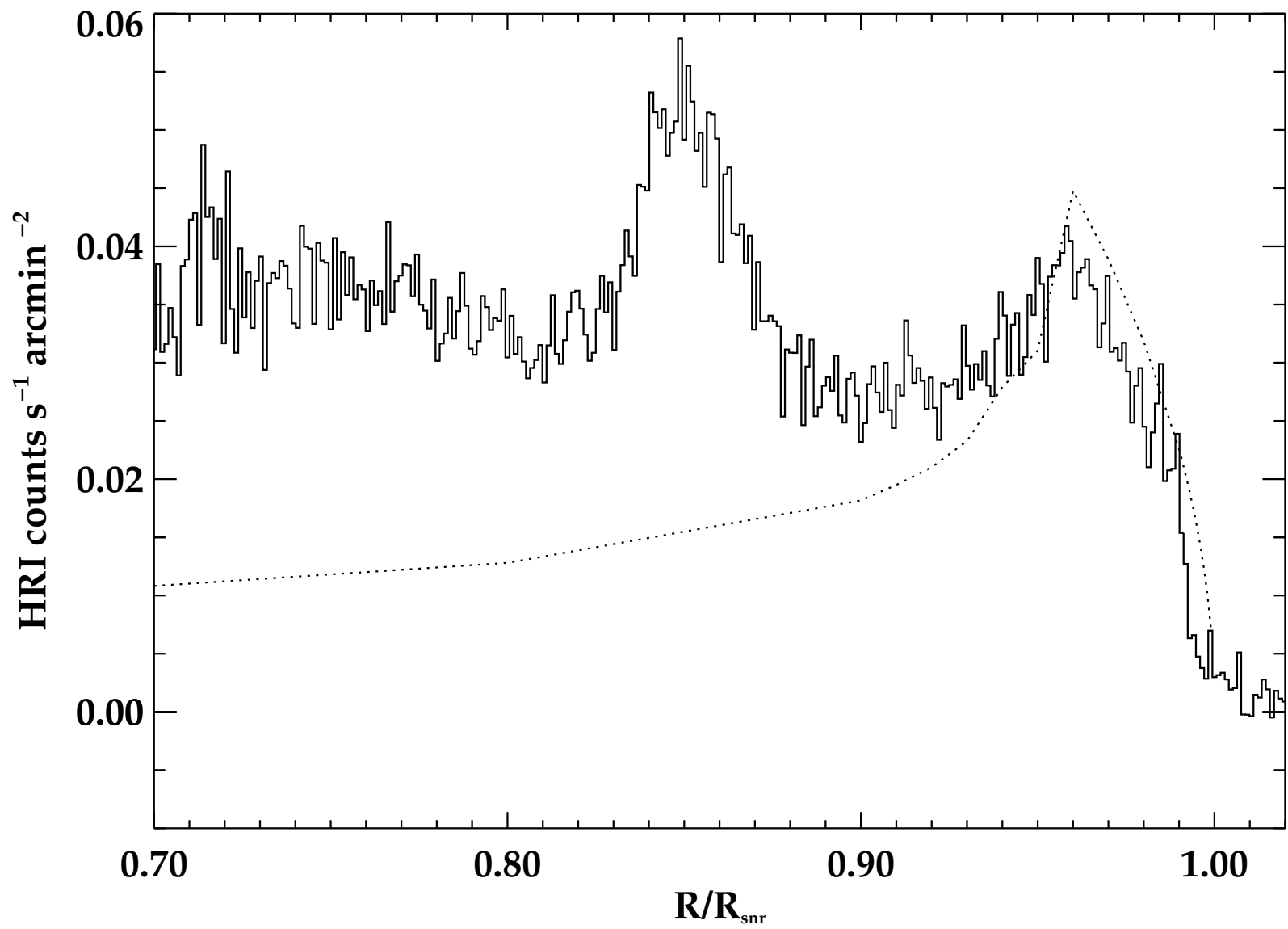
This figure "f7c.jpg" is available in "jpg" format from:

<http://arxiv.org/ps/astro-ph/9703092v1>









The ROSAT-HRI X-Ray Survey of the Cygnus Loop

N. A. Levenson¹, J. R. Graham¹, B. Aschenbach², W. P. Blair³, W. Brinkmann²,
J.-U. Busser², R. Egger², R. A. Fesen⁴, J. J. Hester⁵, S. M. Kahn⁶, R. I. Klein^{1,7},
C. F. McKee^{1,8}, R. Petre⁹, R. Pisarski⁹, J. C. Raymond¹⁰, and S. L. Snowden⁹

ABSTRACT

We describe and report progress on the joint U.S. and German campaign to map the X-ray emission from the entire Cygnus Loop supernova remnant with the ROSAT High Resolution Imager. The Cygnus Loop is the prototype for a supernova remnant that is dominated by interactions with the interstellar medium and supplies fundamental physical information on this basic mechanism for shaping the interstellar medium. The global view that these high-resolution ($FWHM \sim 10''$) observations provide emphasizes the inhomogeneity of the interstellar medium and the pivotal nature of cloud-blast wave interactions in determining the X-ray morphology of the supernova remnant. While investigating the details of the evolution of the blast wave, we also describe the interstellar medium in the vicinity of the Cygnus Loop, which the progenitor star has processed. Although we do not expect the X-ray observations to be complete until September 1997, the incomplete data combined with deep $H\alpha$ images provide definitive evidence that the Cygnus Loop was formed by an explosion within a preexisting cavity.

¹Department of Astronomy, University of California, Berkeley, CA 94720

²Max-Planck-Institut für Extraterrestrische Physik, Giessenbachstrasse, D-85740 Garching, Germany

³The Johns Hopkins University, Department of Physics and Astronomy, Baltimore, MD 21218

⁴Department of Physics and Astronomy, Dartmouth College, Hanover, NH 03755

⁵Department of Physics and Astronomy, Arizona State University, Tempe, AZ 85287

⁶Departments of Astronomy and Physics, Columbia University, New York, New York 10027

⁷Lawrence Livermore National Laboratory, Livermore, CA 94550

⁸Department of Physics, University of California, Berkeley, CA 94720

⁹Goddard Space Flight Center, Greenbelt, MD 20771

¹⁰Center for Astrophysics, 60 Garden St., Cambridge, MA 02138

Subject headings: X-rays:ISM–ISM:individual (Cygnus Loop)–supernova remnants

1. Introduction

Supernova explosions are one of the most basic processes that define the physical and chemical state of the interstellar medium (ISM). The interaction between supernova remnants (SNRs) and the ISM is complex and symbiotic. X-ray observations are important in the study of SNRs because thermal emission from hot material ($kT \sim 0.1\text{--}1$ keV) is the primary tracer of gas that the supernova remnant blast wave heats and accelerates. High resolution X-ray observations are important for studying SNR gas dynamics for three reasons. First, the length scale, ℓ , for cooling and recombination behind a radiative shock is small: $\ell \approx 2.5 \times 10^{17} v_{s7}^4 / n_0$ cm, where n_0 is the preshock number density, and v_{s7} is the shock velocity in units of 100 km s^{-1} (McKee 1987). Second, the preshock medium is not uniform, having clouds and substructure ranging over scales from tens of pc and downward. Third, gas-dynamical instabilities are important, and multi-dimensional hydrodynamic calculations predict that fully developed turbulence occurs when the blast wave collides with an interstellar cloud (Klein, McKee, & Colella 1994; Klein, McKee, & Woods 1995). Consequently, structure is present down to the smallest scales that can be resolved computationally. The improved ROSAT-HRI sensitivity and spatial resolution compared to *Einstein* make it invaluable for exploring cloud-blast wave interactions. The ROSAT-HRI combines high 0.1-2.4 keV sensitivity (approximately three times better than the *Einstein* HRI; Zombeck et al. 1990), high spatial resolution ($FWHM \approx 6''$ on axis), and high contrast imaging (the half-energy radius is $3''$ on axis, with scattering less than a few percent; Aschenbach 1988) to provide a powerful tool for investigating cloud-blast wave interactions.

The region of the Milky Way towards Cygnus is viewed along the Carina-Cygnus arm and exhibits a complex array of bright and dark clouds on the Palomar Sky Survey. Most remarkable are the arcs and loops of faint $H\alpha$ nebulosity, the smallest and brightest of which is the Cygnus Loop ($\ell = 74.0$, $b = -8.6$). The Cygnus Loop is the prototype middle-aged SNR and is a particularly suitable candidate for a case study being nearby (770 pc; Minkowski 1958) and bright with low foreground extinction [$E(B - V) = 0.1$], thus ensuring unrivaled signal-to-noise and spatial resolution. From an observational perspective the Cygnus Loop is unique in terms of X-ray brightness, shock front resolution ($1'' \equiv 1.1 \times 10^{16}$ cm), and interaction with a range of interstellar conditions. The Cygnus

Loop is also at sufficiently high galactic latitude that confusion with background emission from the plane of the galaxy is minimized. Unlike other well-known younger SNRs such as Cas A, Tycho, and Kepler, the structure of the Cygnus Loop is dominated by its interaction with its environment. The large diameter of the Cygnus Loop ($3^\circ \equiv 40$ pc) assures that it is interacting with different components of the ISM, from molecular gas on the northwest edge (Scoville et al. 1977), to diffuse atomic gas along the northeast and eastern limbs (DeNoyer 1975; Hester, Raymond, & Blair 1994), and low density, hot, ionized gas to the south (Ku et al. 1984). Previous studies of the Cygnus Loop have focused on individual regions selected for their brightness or morphological peculiarity (e.g. Hester & Cox 1986, Hester et al. 1994, Fesen, Kwitter & Downes 1992, Graham et al. 1995, and Levenson et al. 1996). The goal of this high-resolution investigation (Graham & Aschenbach 1996) is to make an unbiased survey and thereby establish globally the state of the medium into which the blast wave expands. A coherent picture emerges from our preliminary results (§2). We present a unified interpretation of the environment and development of the Cygnus Loop (§3), constrain the global models that are relevant (§4), and summarize the conclusions in §5.

2. Observational Strategy and Data Reduction

Our primary goal is to map the entire Cygnus Loop remnant at the highest spatial resolution that can be attained with the ROSAT-HRI. Achieving this ambition is not simple, because the spatial resolution is limited by the intrinsic instrumental properties and photon counting statistics. The on-axis resolution is about $6''$, but the off-axis imaging performance is dominated by telescope aberrations, which increase with increasing field angle. At $20'$, the edge of the useful field of view of the HRI, the resolution has degraded to about $30''$. The large range of surface brightness allows us the luxury of mapping the brightest regions at full HRI resolution, but forces us to seek a compromise between effective resolution and observing time in the dimmest regions. To give a concrete example, the surface brightness observed with the ROSAT HRI yields a count rate of 3×10^{-5} – 1×10^{-3} s^{-1} in a $5'' \times 5''$ pixel. For the brightest regions along the shell (within a factor of two of the highest surface brightness) a 15 ks exposure will net 15 counts and 0.4 background counts. It would take longer than 450 ks to obtain a similar number of counts in the faint interior. We therefore adopted the following observing strategy. We use the full $6''$ resolution to observe the brightest regions, which restricts the effective field of view to $8'$ radius. Each of these 24 pointings requires 15–20 ks to obtain 15 counts per pixel. In a comparable exposure time, the moderate surface brightness interior regions yield about 10 counts per $12'' \times 12''$ pixel. At this resolution, the effective HRI field of view has a $12'$ radius. We have observed

these nine fields for 20–25 ks. Observing the low surface brightness regions, we obtain 10 counts per cell only when using a 15" or larger pixels, for which the full HRI field of view is suitable. Each of these 10 fields requires a 35 ks exposure. Finally, one very low surface brightness region along the western edge of the “breakout” requires a 50 ks exposure to obtain reliable counting statistics. The locations of the HRI pointings are shown on the *Einstein* IPC map (Fig. 1).

A few fields were observed during the initial operation of ROSAT, and a concerted effort to make a complete map began during AO5, in October 1994. Because of the large total observing time this program requires, it is a collaborative project between U.S. and German investigators. So far 771 ks out of a total 1066 ks of data have been obtained and we expect completion in AO7, by September 1997. The complete mosaic will consist of 47, fields of which 37 have been observed at least in part. We present processed data for 26 fields, of which 15 are complete. The target names, field centers, and exposure times are listed in Table 1, and the observations that are presented here appear first. Column 4 contains the live time, which is the useful portion of the observations, and column 5 lists the remainder of the requested time.

The data were processed and combined into a single image using software designed to analyze extended sources and the diffuse background (Snowden et al. 1994). Over such large spatial scales, each observation is a distinct projection of the sky onto the plane of the detector, and these must be re-mapped to a common projection. For each observation, using only the accepted time intervals listed in the raw data files, three images are created. The first map contains the total counts, the second map is a model of particle background, and the third is an exposure map, which includes the variations in the detector quantum efficiency. These images have 5" pixels, matching the instrument’s angular resolution. These maps from individual fields are summed on a pixel-by-pixel basis into three mosaics of the entire Cygnus Loop field. For the initial analysis we present here, we use a uniform pixel scale and field of view from each observation. Only the central 17' of each observation in order to avoid the significant degradation of the point spread function and decreased efficiency at large off-axis angles, except for two fields where a radius of 20' was used to avoid a gap in the resulting image. The count rate map (Fig. 2) has 15" pixels and is the difference of the total counts and the total background, divided by the net exposure (Fig. 3). Background subtraction is not a problem for the bright and moderately bright fields, but the background does become comparable with the source surface brightness for the lower surface brightness regions. The extent of the observations is demonstrated in Figure 4, where the individual image boundaries are drawn on the count rate map.

To display the high resolution information contained in the mosaic, we also show three

smaller fields that have been binned with $6''$ pixels (Figs. 5a, 6a, and 7a). For comparison, we present aligned optical images of the same regions taken through a narrow $H\alpha$ filter (Figs. 5b, 6b, and 7b). These were obtained using the Prime Focus Corrector on the 0.8 m telescope at McDonald Observatory and are described in Levenson et al. (1997). After basic reduction consisting of bias subtraction and flat-fielding, individual images were re-mapped and averaged using the same technique that was applied to the X-ray observations. Figures 5c, 6c, and 7c are color versions of these combined data sets to show the relative spatial distributions directly.

3. Results

The X-ray morphology of a SNR is a primary diagnostic of the medium into which the blast wave propagates. At first sight the X-ray morphology depicted in the ROSAT-HRI mosaic presents a bewilderingly complex view. This shows *prima facie* that the Cygnus Loop is dominated by its interaction with an inhomogeneous environment. In contrast, we note also that the Cygnus Loop appears nearly circular except for the breakout region to the south, which suggests that the SNR expands in a uniform medium. Any model for the Cygnus Loop must resolve this apparent paradox.

There is considerable large- and small-scale azimuthal variation around the perimeter of the Cygnus Loop and significant structure projected across its face. X-ray emission is bright near the rim, but the brightest peaks all lie interior to the circle that circumscribes the X-ray edge. The two most prominent X-ray regions, NGC 6960 on the western edge and NGC 6992 to the northeast, lie at the largest projected distance inside this circle. These regions contain complex networks of X-ray filaments and high surface brightness clumps. The emission here is strongly limb brightened. Figures 8 and 9 show radial cuts of the emission from these regions. The limb-brightening (i.e. the ratio of brightness at center to edge) is about a factor of 6 in the northeast (Fig. 8) and 30 in the west (Fig. 9). The adiabatic expansion of a supernova blast wave in a uniform medium results in some degree of limb brightened X-ray emission but is inadequate to account for these profiles. We have calculated the X-ray surface brightness profile (Fig. 10) using the Sedov density profile (Sedov 1993), taking X-ray volume emissivity to be proportional to density squared, and assuming that it is independent of temperature, which is reasonable for the energy coverage of our observations (Hamilton, Sarazin, & Chevalier 1983). The maximum limb-brightening is 3.3 and occurs near the edge of the SNR. The clear message from this comparison is that the observed X-ray profiles in these bright regions of the Cygnus Loop have peaks in the wrong place and too great in contrast to be the result of an adiabatic blast wave

propagating in a uniform medium. Thermal evaporation does not explain the X-ray profiles either, as the evaporative solutions of White & Long (1991) demonstrate (Fig. 10; see also Cowie, McKee, & Ostriker 1981). The effect of thermal conduction is to provide more mass farther behind the blast wave, so these solutions always exhibit less extreme limb brightening than the adiabatic case. *The Cygnus Loop is neither a Sedov remnant nor a Sedov remnant modified by thermal evaporation.*

3.1. X-ray and Optical Correlations

Optical line emission alone reveals some details of shock structure. For example, faint $H\alpha$ filaments trace the progress of the blast wave in neutral gas, [O III] emission reveals where postshock gas first starts to cool and recombine, and [S II] and bright $H\alpha$ together show where complete cooling and recombination zones have developed. Utilizing X-ray and optical information together, however, provides a more complete understanding of the structure and development of supernova remnant shocks.

The observed correlation between X-ray and optical line emission falls into three broad categories that are distinguished by surface brightness and morphology: (1) regions of high surface brightness X-ray emission distributed in long coherent arcs that are aligned tangentially with, and lie interior to, the bright optical filaments; (2) localized indentations in the shell, typically less than $20'$ in size, where bright X-ray emission occurs at large distances behind the projected edge of the blast wave; and (3) regions of low surface brightness, limb-brightened X-rays bounded on the outside by faint, narrow Balmer-line filaments.

Examples of type (1) morphology are NGC 6992 in the northeast ($\alpha = 20^{\text{h}}56^{\text{m}}, \delta = +32^\circ$, J2000) and NGC 6960 on the western edge ($20^{\text{h}}46^{\text{m}}, +31^\circ$). Type (2) regions are found on the eastern edge ($20^{\text{h}}57^{\text{m}}, +31^\circ$), the southeast cloud ($20^{\text{h}}56^{\text{m}}, +31^\circ$), and the bright funnel-shaped section ($20^{\text{h}}50^{\text{m}}, +32^\circ$) that is located about $30'$ northeast of the optical emission region known as the “carrot” (Fesen, Blair, & Kirshner 1982). These regions tend to be more turbulent and include the most compact and highest surface brightness knots within the Cygnus Loop. Categories (1) and (2) occur where the shock has encountered a greater than average column of gas, which has caused substantial deceleration of the blast wave (Hester & Cox 1986; Hester et al. 1994; Graham et al. 1995; Levenson et al. 1996). The difference between regions (1) and (2) may be due to viewing geometry, the shape of the cloud which is being encountered, and the time since enhanced density was encountered by the shock. The western edge provides a vivid example of a blast wave-cloud interaction because this region is viewed almost exactly edge-on, minimizing the

complications of projection effects (Levenson et al. 1996). The best examples of type (3) filaments occur at the extreme north ($20^{\text{h}}54^{\text{m}}, +32^{\circ}$), to the south of the southeast knot, and to the north of NGC 6960. These filaments show the location of the current projected edge of the blast wave because Balmer-line filaments occur where previously undisturbed atomic gas is shocked (Chevalier & Raymond 1978; Chevalier, Kirshner, & Raymond 1980; Hester, Danielson, & Raymond 1986). The X-rays do not completely overlap the optical emission but are offset to the interior. We measure offsets of $5 - 20''$ between the exterior edge of X-ray emission and the edge of the Balmer filaments; offsets of $10''$ (equivalent to 10^{17} cm) are typical. The separation between the X-ray and optical emission is likely due to the time required to heat the gas behind the shock front before X-rays are emitted. For a shock of velocity $v_s = 400 \text{ km s}^{-1}$, an offset of $20''$ implies a heating time of about 200 yr. This is consistent with Coulomb collisions alone equilibrating the postshock ion and electron temperatures (Spitzer 1962). If the blast wave has decelerated in dense gas where the Balmer filaments are detected, the same separation from the X-ray edge implies that a longer time has elapsed, so Coulomb equilibration alone is still a possible heating mechanism. Whether Coulomb collisions or some other mechanism heat the post-shock electrons, long equilibration timescales are expected, as Laming et al. (1996) demonstrate in analysis of a non-radiative shock observed in SN 1006.

4. A Global View

4.1. Cavity Explosion

Various X-ray studies have successfully discussed individual regions of the Cygnus Loop in terms of blast wave-cloud collisions (e.g. Hester & Cox 1986, Hester et al. 1994, Graham et al. 1995, Levenson et al. 1996), and it is well established that large-scale collisions fundamentally determine the morphology of portions of this supernova remnant. However, the examination of particular regions does not lead to an understanding of the global environment in which the SNR evolves. Specifically, it is important to determine whether the clouds that have been struck by the blast wave are isolated and part of a random distribution or part of a coherent structure, such as an H II region cavity or wind blown bubble formed by the supernova progenitor. Previous global models of the Cygnus Loop (e.g. Falle & Garlick 1982; Tenorio-Tagle, Rozyczka, & Yorke 1985) ignore the evidence for and effects of encounters with clouds and instead model a SNR breaking out of a molecular cloud. On the contrary, these X-ray observations emphasize that over large scales the blast wave is running into dense material, not expanding into a contrasting lower density region.

With the data presented here, it is clear that the Cygnus Loop is the result of a cavity

explosion. The observations of the interior are consistent with blast wave propagation through a rather smooth, low-density medium, and at the periphery, the edge of the cavity has been encountered. The enhancements in the ROSAT X-ray data show that the blast wave is currently interacting with denser material—denser than the medium through which it previously propagated—over 80% of the perimeter that we have observed. Some of these enhancements are narrow, tangential filaments, while others are the large structures that had been identified in earlier observations. Such extensive clumps of material cannot be characteristic of the pre-supernova ISM within the current remnant and thus distinguish the cavity boundary. We observe the cavity walls in these data! Only two extended sites, near $\alpha = 20^{\text{h}}48^{\text{m}}, \delta = +32^{\circ}10'$, and $\alpha = 20^{\text{h}}57^{\text{m}}, \delta = +30^{\circ}30'$, show no evidence for blast wave interaction with the cavity wall.

The cavity walls are nearly complete, consisting of a neutral shell as well as large clouds. When the blast wave reaches the dense atomic shell, it decelerates. The Balmer-dominated filaments directly trace the motion of the blast wave in the atomic gas of the shell. The X-ray signature of this category (3) morphology (cf. §3.1) is enhancement at the SNR edge, where gas is piled up behind the slowing shock. Figures 8, 9, and 11 provide examples of this characteristic X-ray profile in three different locations, where the enhancement occurs at radii of $0.98R_{\text{snr}}, 0.98R_{\text{snr}},$ and $0.96R_{\text{snr}},$ respectively. These enhancements are not due to the global expansion of the blast wave in a uniform medium or evaporation in a uniform distribution of clouds. They are too slight, too limited in radial extent, and misplaced relative to the Sedov and evaporative model predictions. The Balmer filaments and associated X-rays are detected over half the perimeter of the SNR, indicating that blast wave deceleration in atomic material is common. Some regions exhibit the type (3) X-ray signature but the corresponding optical filaments are too faint to be detected. Although the blast wave edge is not directly observed in these cases, the prevalence of category (3) and the observed X-ray morphology imply that the blast wave is decelerating in the dense cavity wall in these locations, as well.

A radial profile across the northwestern edge ($20^{\text{h}}46^{\text{m}}, +31^{\circ}40'$) emphasizes the type (3) X-ray limb-brightening and avoids confusion with emission due to interactions with large clumps (Fig. 11). There is no extended bright optical emission due to radiative shocks near the edge, and this is not a particularly bright region of the X-ray map. Two components are obvious, corresponding to two overlapping projections of the blast wave that are not necessarily physically related. We neglect the interior component and model the exterior component very simply as a shock that strikes a density discontinuity and generates a reflected shock. The Rankine-Hugoniot jump conditions determine the relationship among the flow variables in different regions. The free parameters of the model are the density contrast and its initial location, from which the density profile due the projected and

reflected shocks as a function of radius is calculated. In the Cygnus Loop, Balmer-dominated filaments are typically observed propagating through regions of $n \sim 1 \text{ cm}^{-3}$ (e.g. Hester et al. 1994, Raymond et al. 1983), while in the former H II region cavity $n \sim 0.1 \text{ cm}^{-3}$, so the density contrast is taken to be 10. (This is likely to be an overestimate, however, because the brightest Balmer filaments were analyzed, and these are the ones that have evolved most toward the radiative stage.) The radius of the SNR blast wave is fixed at the location of the Balmer emission. The interior edge of the X-ray enhancement marks the location of the reflected shock. We measure this to be at $R = 0.94R_{snr}$, so the blast wave initially encountered the wall at $R = 0.96R_{snr}$ and is now at $R = 1.0R_{snr}$. Similar to all the model calculations presented here, the X-ray surface brightness profile is computed for the spherically symmetric case (Fig. 11), assuming that X-ray volume emissivity is proportional to density squared and is independent of temperature. This simple model reasonably matches the shape and location of the X-ray enhancement, although this is not a fit to the data. The model does not allow for heating time, so it predicts emission toward the edge of the SNR blast wave that we do not detect. Despite these approximations, however, the simple model indicates the scales of the parameters that cause the X-ray enhancement at the edge where the blast wave has run into the atomic cavity wall.

Several observed properties of the Cygnus Loop argue for a large-scale cavity explosion. The first is the approximate spherical symmetry of the emission. This symmetry of the Cygnus Loop is surprising in view of the rich X-ray morphology, which argues for an inhomogeneous medium. If the inhomogeneity were in the form of a random distribution of clouds, then the clouds would have to be very small in order to account for the fact that the observed gas produces few, if any, significant indentations into the remnant (McKee & Cowie 1975). There are no entirely concave sections on scales greater than $20'$ (4 pc) and no evidence for thermal evaporation of large clouds on the interior, for example. However, X-ray studies of individual regions show that the clouds are quite extended along the periphery of the remnant, with sizes of about 0.5° (7 pc). The clouds are preferentially aligned parallel to the blast wave. In this case, a spherical remnant can be produced only if neither the shape nor the distribution of the clouds is random. To produce a spherical remnant, the clouds in the vicinity of the Cygnus Loop must be located at the edge of the current shell, and they must be flattened along the shell. There is also dynamical evidence that these are the first large clouds that have been encountered by the blast wave: the blast wave-cloud interactions to the northeast and the west are recent and approximately the same age (Hester et al. 1994, Levenson et al. 1996). This conclusion is consistent with that of Charles, Kahn, & McKee (1985), who determined that data are inconsistent with an explosion in a uniform distribution of clouds based on Einstein-IPC observations adjacent to NGC 6960. They suggested that the ISM within the current filamentary ring lacked

clouds before the supernova explosion.

4.2. Progenitor Modification of the ISM

The modification of the SNR environment by the pre-supernova star has been discussed by McKee, Van Buren, & Lazareff (1984) and Shull et al. (1985). If the progenitor star of the Cygnus Loop SNR were an early B star, then the Lyman continuum radiation from this main-sequence star created an H II region. In the warm neutral interstellar medium with average density distribution $n \approx 0.2 \exp(-z/220 \text{ pc}) \text{ cm}^{-3}$ (Kulkarni & Heiles 1988), a star at height $z = 120 \text{ pc}$ emitting Lyman continuum photons at a rate of 10^{46} s^{-1} creates an H II region with a density of about 0.1 cm^{-3} and a radius of about 30 pc . As denser clumps of gas within the H II region are photoevaporated, adding more material to the ionized interior, the radius of the H II region decreases. Small clouds are ultimately destroyed by photoevaporation and larger clouds are driven away by the rocket effect (Bertoldi & McKee 1990). The details of the photoevaporation depend on the velocity of the progenitor star and on the properties of the clouds: temperature, density, and magnetic field. Using Bertoldi's (1989) results, one can show that atomic clouds ($T \sim 10^2 \text{ K}$) in pressure balance with the H II region ($P/k \sim 2000 \text{ K cm}^{-3}$ for $n_{H II} \sim 0.1 \text{ cm}^{-3}$) will be either destroyed or rocketed out of the H II region. Molecular clouds are more difficult to destroy by photoevaporation (Shull et al. 1985), but at the distance of the Cygnus Loop below the plane, very large molecular clouds are unlikely. As a result of photoevaporation and photodissociation, a dense atomic shell that contains most of the mass surrounds the H II region, which is bounded by a recombination front. A vigorous wind may aid formation of the shell, although this is unlikely in the case of an early B star we consider here. Once the progenitor leaves the main-sequence and becomes a red giant, the H II region begins to recombine, but the density is too low for much recombination to occur before the star explodes.

When the progenitor of the Cygnus Loop became a supernova, the blast wave initially expanded adiabatically through the diffuse cavity gas. Eventually it hit the walls of the cavity, which are comprised of the surrounding atomic shell and the remains of clouds that protrude into the H II region. NGC 6960 is a clear example where the blast wave has encountered dense molecular gas (Levenson et al. 1996). The eastern edge and the southeast cloud may be additional examples of elephant-trunk structures, such as those observed in M 16 (e.g. Hester et al. 1996), protruding into the shell (Graham et al. 1995). The existence of large clouds near the cavity edge is expected, for the development of an H II region tends to homogenize its interior, while its action on the boundary is limited by

intervening clouds along the same line of sight and decreased ionizing flux at larger radii. The clouds currently at the edge were either rocketed out of the interior or were originally located at the periphery of the H II region.

We have considered a progenitor of spectral type later than B0 because a stationary star of earlier spectral type star would homogenize an H II region to a radius of about 50 pc, while there are clearly inhomogeneities within the present 20 pc extent of the SNR (McKee et al. 1984; Charles et al. 1985). If a massive star is moving, however, the clouds situated perpendicular to its path are not exposed to the Lyman continuum emission for as long. The rocket effect and photoevaporation are less effective on these clouds, and the homogenizing radius across the direction of motion is reduced. Along the direction of motion, the distribution of the processed interstellar medium is anisotropic: toward the original location of the progenitor, gas has been exposed to ionizing radiation, so it is more homogeneous and less dense, while the processing is limited in the direction that the star moves, so the ISM is clumpier and less dense there. The progenitor of the Cygnus Loop would have been later than B0, provided that it was not moving too rapidly; ($v_* \lesssim$ a few km s^{-1} so that surrounding clouds are exposed to the ionizing radiation for a time $R/v_* \gtrsim 6 \times 10^6$ yr). Alternatively, an earlier-type progenitor is possible provided that it was moving predominantly along our line of sight. In this case, the projected edge of the cavity would still be circular, yet have a smaller radius than one carved by a stationary star.

5. Conclusions

The density inhomogeneities around the Cygnus Loop determine not only the appearance of the SNR at optical and X-ray wavelengths, but also they fundamentally alter the blast wave development. The consequences are significant beyond this single example. Global models of the interstellar medium that assume the clouds around supernova remnants are insignificant or rely on statistical measures such as the number-diameter relation must be revised.

The high-resolution, global view of the Cygnus Loop these data provide resolves the apparent paradox of the Cygnus Loop: a near-circular shape and evidence for interaction with large-scale inhomogeneities in the interstellar medium. The X-ray data make clear that the blast wave has recently encountered density enhancements, which we identify as the walls of a cavity. The H II region of the progenitor star worked to homogenize a spherical cavity with ionizing radiation, and the blast wave initially propagated through this cavity, maintaining its spherical symmetry. Marking the edge of the cavity is a dense shell of atomic gas and large clumps of the processed surrounding medium or formerly

interior clouds that were rocketed out. Portions of the blast wave have been decelerated in the smooth atomic shell, which Balmer-dominated filaments and slightly limb-brightened X-ray profiles trace. Other sections of the blast wave have swept up even larger column densities, resulting in very bright X-rays and optical emission. The observed features of the Cygnus Loop are expected rather than surprising in the context of stellar evolution that preceded the supernova.

We thank the USRSDC for providing the ESAS software used to reduce the X-ray data. The optical images were obtained using the Prime Focus Corrector on the 0.8-m telescope at McDonald Observatory in collaboration with L. Keller and M. J. Richter. The research of CFM is supported in part by NSF grant AST95-30480.

REFERENCES

- Aschenbach, B. 1988, *Appl. Opt.*, 27, 1404
- Bertoldi, F. 1989, *ApJ*, 346, 735
- Bertoldi, F., & McKee, C. F. 1990, *ApJ*, 354, 529
- Charles, P. A., Kahn, S. M., & McKee, C. F. 1985, *ApJ*, 295, 456
- Chevalier, R. A., Kirshner, R. P., & Raymond, J. C. 1980, *ApJ*, 235, 186
- Chevalier, R. A., & Raymond, J. C. 1978, *ApJ*, 225, L27
- Cowie, L. L., McKee, C. F., & Ostriker, J. P. 1981, *ApJ*, 247, 908
- DeNoyer, L. K. 1975, *ApJ*, 196, 479
- Falle, S. A. E. G., & Garlick, A. R. 1982, *MNRAS*, 201, 635
- Fesen, R. A., Blair, W. P., & Kirshner, R. P. 1982, *ApJ*, 262, 171
- Fesen, R. A., Kwitter, K. B., & Downes, R. A. 1992, *AJ*, 104, 719
- Graham, J. R. & Aschenbach, B. 1996, in *ROSAT Newsletter #13*, Ed. S. L. Snowden, 6
- Graham, J. R., Levenson, N. A., Hester, J. J., Raymond, J. C., & Petre, R. 1995, *ApJ*, 444, 787
- Hamilton, A. J. S., Sarazin, C. L., & Chevalier, R. A. 1983, *ApJS*, 51, 115
- Hester et al. 1996, *AJ*, 111, 2349
- Hester, J. J., & Cox, D. P. 1986, *ApJ*, 300, 675
- Hester, J. J., Danielson, G. E., & Raymond, J. C. 1986, *ApJ*, 303, L17

- Hester, J. J., Raymond, J. C. & Blair, W. P. 1994, *ApJ*, 420, 721
- Klein, R. I., McKee, C. F., & Colella, P. 1994, *ApJ*, 420, 213
- Klein, R. I., McKee, C. F., & Woods, D. T. 1995, in *The Physics of the Interstellar Medium and Intergalactic Medium*, ed. A. Ferrara, C. F. McKee, C. Heiles, and P. R. Shapiro (San Francisco: ASP), 366
- Ku, W. H.-M., Kahn, S. M., Pisarski, R. & Long, K. S. 1984, *ApJ*, 278, 615
- Kulkarni, S. R., & Heiles, C. 1988, in *Galactic and Extragalactic Radio Astronomy*, 2nd ed., ed. G. L. Verschuur and K. I. Kellermann, (New York: Springer-Verlag), 95
- Laming, J. M., Raymond, J. C., McLaughlin, B. M., & Blair, W. P. 1996, *ApJ*, 472, 267
- Levenson, N. A., Graham, J. R., Hester, J. J., & Petre, R. 1996, *ApJ*, 468, 323
- Levenson, N. A., Graham, J. R., Keller, L., & Richter, M. J. 1997, in preparation
- McKee, C. F. 1987, in *Spectroscopy of Astrophysical Plasmas*, ed. A. Dalgarno and D. Layzer, (New York: Cambridge University Press.), 226
- McKee, C. F. & Cowie, L. L. 1975, *ApJ*, 195, 715
- McKee, C. F., Van Buren, D. & Lazareff, B. 1984, *ApJ*, 278, L115
- Minkowski, R. 1958, *Rev. Mod. Phys.*, 30, 1048
- Raymond, J. C., Blair, W. P., Fesen, R. A., & Gull, T. R. 1983, *ApJ*, 275, 636
- Scoville, N. Z., Irvine, W. M., Wannier, P. G., & Predmore, C. R. 1977, *ApJ*, 216, 320
- Sedov, L. I. 1993, *Similarity and Dimensional Methods in Mechanics*, 10th ed., (Boca Raton: CRC Press)
- Seward, F. D. 1990, *ApJS*, 73, 781
- Shull, P., Jr., Dyson, J. E., Kahn, F. D., & West, K. A. 1985, *MNRAS*, 212, 799
- Snowden, S. L., McCammon, D., Burrows, D. N., & Mendenhall, J. A. 1994, *ApJ*, 424, 714
- Spitzer, L., Jr. 1962, *Physics of Fully Ionized Gases*, 2nd ed., (New York: Wiley)
- Tenorio-Tagle, G., Rozyczka, M., and Yorke, H. W., 1985, *A&A*, 148, 52
- White, R. L., & Long, K. S. 1991, *ApJ*, 373, 543
- Zombeck, M. V., et al. 1990, *Proc. SPIE*, 1344, 267

Fig. 1.— ROSAT-HRI pointings superposed on the *Einstein* IPC image of the Cygnus Loop (Seward 1990). Solid circles indicate fields that are presented in this paper; dashed circles show unprocessed or proposed observations.

Fig. 2.— ROSAT-HRI count rate map of the Cygnus Loop. This image is a mosaic of 41 pointings in 26 positions. Each observation has been background-subtracted and exposure-corrected before being combined into this map, which has $15''$ pixels. It is scaled linearly from 0 to $0.15 \text{ counts s}^{-1}\text{arcmin}^{-2}$.

Fig. 3.— Exposure map of combined ROSAT-HRI observations, including detector variations.

Fig. 4.— The boundaries of individual pointings are shown on the ROSAT-HRI count rate mosaic of the Cygnus Loop. The sharp, nearly circular edge of the supernova remnant is real, not an artifact of the limited extent of the observations.

Fig. 5.— The northeast rim of the Cygnus Loop at $6''$ resolution. (a)HRI data, which exhibits three distinct types of X-ray emission: long filaments of bright emission, spots of extremely bright emission accompanied by indentations in the X-ray shell, and fainter limb-brightened filaments. (b)The northeast rim of the Cygnus Loop in $\text{H}\alpha$, scaled linearly. The optical image contains extended radiative filaments, small spots of bright emission, and long, faint filaments due to Balmer-dominated shocks, corresponding to the classes of X-ray emission. (c)False-color composite of HRI (green) and $\text{H}\alpha$ (red) observations, illustrating the exact relation between the X-ray and optical emission. The optical image has been median-filtered to remove stars.

Fig. 6.— The southeast region of the Cygnus Loop at $6''$ resolution. (a)HRI, (b) $\text{H}\alpha$, and (c) false-color composite, as in Figure 5.

Fig. 7.— The northwest edge of the Cygnus Loop at $6''$ resolution. (a)HRI, (b) $\text{H}\alpha$, and (c) false-color composite, as in Figure 5.

Fig. 8.— HRI surface brightness as a function of radius across the bright northeastern rim of the Cygnus Loop. This radial profile is an azimuthal average over $2'$. Very bright emission appears projected to the interior of the SNR and extends over more than 12% of its radius. While there is no significant X-ray emission at the edge of the SNR, fainter X-ray limb-brightening appears to the interior, at $R = 0.98R_{snr}$. (Balmer-dominated optical filaments define the edge of the SNR that is indicated in Figures 8, 9, and 11.) This X-ray emission is clearly distinct from that due to expansion of a blast wave in a uniform medium (cf. Fig. 10).

Fig. 9.— HRI surface brightness as a function of radius across the bright western rim of the Cygnus Loop, azimuthally averaged over $2'$. Extremely bright emission appears projected to the interior of the SNR, at $R = 0.92R_{snr}$. Significant, though less extreme, limb-brightening is also observed at $R = 0.98R_{snr}$.

Fig. 10.— Model X-ray surface brightness profiles for Sedov SNR (solid line) and evaporative cloud model of White & Long (1991; dotted line) with their parameters $C = 10$ and $\tau = 10$. Both profiles have been normalized to a uniform level at the center of the supernova remnant.

Fig. 11.— HRI surface brightness as a function of radius across the northwestern rim of the Cygnus Loop, azimuthally averaged over $2'$. Two separate components of the limb-brightened shell are evident, near $R = 0.96R_{snr}$ and $R = 0.85R_{snr}$. Both components are the result of interaction of the blast wave with the cavity wall, although the latter appears projected to the interior of the SNR. The outer peak is modeled as the result of a density contrast and reflected shock (dotted line). In this model, the blast encounters a density contrast of 10 at $R = 0.96R_{snr}$ and the reflected shock has progressed to $R = 0.94R_{snr}$ when the forward shock has reached $R = 1.0R_{snr}$.

TABLE 1
HRI OBSERVATIONS

Name	α (J2000)	δ (J2000)	Time (ks)	
			Live	Remaining
WEST	20 ^h 45 ^m 41 ^s	31° 02' 23''	29.2	0
W RIM 4	20 45 53	31 27 36	17.6	0
W RIM 3	20 46 48	31 45 36	13.0	6.9
SW CLOUD	20 47 50	29 18 00	46.4	0
W RIM 2	20 47 55	32 02 23	10.1	4.9
NORTH	20 50 02	32 11 23	16.0	0
E RIM 1	20 51 31	32 19 12	16.5	0
CENTER	20 51 53	31 07 12	11.9	13.1
SE INT 2	20 52 31	30 06 36	25.7	9.3
E RIM 11	20 52 50	29 23 59	19.1	0
E RIM 2	20 52 58	32 18 36	10.2	4.8
E RIM 10	20 53 31	29 43 48	21.1	0
NE INT 1	20 53 41	31 51 00	17.0	3.0
E RIM 3	20 54 29	32 15 00	11.1	3.9
SE INT 1	20 54 34	30 28 12	26.8	8.2
E RIM 9	20 54 36	29 56 59	14.8	0
NE INT 2	20 54 58	31 32 23	14.2	5.8
NE INT 4	20 55 24	30 40 12	18.6	0
NE INT 3	20 55 34	31 08 59	18.9	0
E RIM 4	20 55 41	31 58 48	12.6	0
E RIM 8	20 55 58	30 04 12	14.3	0
SE CLOUD	20 56 22	30 23 59	28.3	0
E RIM 7	20 56 31	30 42 36	11.5	3.5
E RIM 5	20 56 46	31 43 11	11.9	3.1
EAST	20 57 17	31 02 23	30.1	0
E RIM 6	20 57 29	31 25 12	15.9	0
W RIM 6	20 46 07	30 25 48	0	20.0
W RIM 7	20 47 02	30 09 00	0	20.0
W RIM 5	20 47 23	31 27 00	0	20.0
NW INT	20 47 28	31 26 55	0	15.0
W RIM 8	20 47 48	29 51 00	0	20.0
W INT 1	20 47 55	31 00 00	0	35.0
W INT 2	20 48 05	30 31 48	0	35.0
W RIM 9	20 48 50	29 37 48	0	20.0
W INT 3	20 48 55	30 11 31	0	35.0
W RIM 1	20 49 04	32 14 06	0	20.0
INT 1	20 49 34	31 22 01	0	25.0
W INT 4	20 50 03	30 49 30	0	35.0
W INT 5	20 50 27	30 18 28	0	35.0
N INT 2	20 50 28	31 49 26	0	20.0
BREAK	20 50 41	29 13 48	0	35.0
W INT 6	20 50 49	29 44 31	0	35.0
N INT 1	20 51 27	31 57 32	0	15.0
N INT 3	20 51 44	31 38 16	0	20.0
SE INT 3	20 52 07	30 34 48	0	35.0
NE INT 5	20 53 24	31 11 12	0	25.0
NE INT 6	20 53 41	30 58 12	0	25.0